

Cite this: *J. Mater. Chem. A*, 2022, 10, 18845

N-doping of nonfullerene bulk-heterojunction organic solar cells strengthens photogeneration and exciton dissociation†

Jiaqi Xie, ^a Weihua Lin, ^b Guillermo C. Bazan, ^c Tõnu Pullerits, ^b Kaibo Zheng ^{*bd} and Ziqi Liang ^{*a}

N-type doping of the bulk-heterojunction layer in nonfullerene organic solar cells allows to effectively ameliorate inferior electron transportation by filling traps and optimizing electron pathways, leading to a better balance of charge transport in device. This mechanism, however, provides an incomplete understanding of the stronger photogeneration, long-lived excitons and simultaneously increased short-circuit current density (J_{SC}) and open-circuit voltage (V_{OC}) that also benefit from the n-doping. Herein we investigate how molecular n-dopant impacts the optical characteristics, intermolecular packing behavior, charge carrier dynamics and photovoltaic performance in the nonfullerene-based blend. When incorporating a prototypical n-type dopant N-DMBI into a benchmark PM6:Y6 blend, the crystallization of PM6/Y6 is facilitated and the crystal coherence length is elongated, which is correlated with the optical absorbance enhancement. N-doping is unveiled to prolong exciton lifetime by retarding geminate recombination (GR) both at donor/acceptor (D/A) interfaces and within constituent domains by dilating interspace, reducing trap states and decreasing exciton binding energy. Despite slower interfacial charge transfer across the enlarged D/A interspace due to dopant intercalation, exciton dissociation remains highly effective due to the impeded interfacial GR. Consequently, the champion inverted cell at an optimal N-DMBI content delivers a decent efficiency of 15.34%, which is among the highest of the state-of-the-art analogous PM6:Y6-based binary cells. Such improvement is largely ascribed to the concurrent increase of J_{SC} (up to 26.41 mA cm⁻²) and V_{OC} (up to 0.86 V) in comparison to the undoped device.

Received 26th June 2022
Accepted 14th August 2022

DOI: 10.1039/d2ta05078a

rsc.li/materials-a

Introduction

Molecular doping has manifested as a direct approach to tune the optoelectronic properties of organic semiconductors, for which there are two paradigm mechanisms for the interactions between dopant and host: (i) strong redox reaction with integral charge transfer under sufficient energy-level offsets and (ii) weak molecular orbital hybridization with partial charge transfer among interactive moieties.^{1,2} In organic solar cells (OSCs), molecular doping of the bulk-heterojunction (BHJ) active layer allows for tailoring the electronic structure to promote photoinduced charge generation and transport

processes, whereas the conventional additive engineering in OSCs is more prone to the morphological improvement.^{3,4} It has become recognized that molecular dopants (both p- and n-types) possess dual-functionality to modulate not only the electronic properties but also the microstructures of the BHJ layer in OSCs. On the one hand, extra free carriers brought from the dopant would increase the background charge carrier density to fill deep-level traps,⁵ enhance interfacial electric field to assist in exciton splitting,⁶ create more interfacial bridging states to improve photo-charge-generation yield,⁷ *etc.* On the other side, a small quantity of molecular dopant was shown to increase thin-film crystallinity, which is favorable for charge transportation.^{4,8-10} However, a high doping level in BHJ layers is often undesired since the coulombic potential of dopant counterions can create additional traps and thereby diminish the long-range order of molecular packing,^{11,12} which serves as a bottleneck to increasing electrical conductivity and preventing over-high dark carrier density.¹³ In principle, n- or p-doping are both feasible in electron acceptors and donors, respectively, yet n-doping in OSCs is remarkably more challenging due to limited candidate dopants, mismatched energy levels and air instability.^{4,8}

^aDepartment of Materials Science, Fudan University, Shanghai 200433, China. E-mail: zqliang@fudan.edu.cn

^bDepartment of Chemical Physics and NanoLund, Lund University, Box 124, 22100 Lund, Sweden

^cDepartment of Chemistry, National University of Singapore, Singapore 117543, Singapore

^dDepartment of Chemistry, Technical University of Denmark, DK-2800 Kongens Lyngby, Denmark. E-mail: kzheng@kemi.dtu.dk

† Electronic supplementary information (ESI) available. See <https://doi.org/10.1039/d2ta05078a>

Since the Zhan group pioneered the design of the first non-fullerene acceptor (NFA), 3,9-bis(2-methylene-(3-(1,1-dicyanomethylene)-indanone))-5,5,11,11-tetrakis(4-hexylphenyl)-dithieno[2,3-*d*:2',3'-*d'*]-*s*-indaceno[1,2-*b*:5,6-*b'*]dithiophene (ITIC), in 2015, recent years have witnessed unparalleled advances in NFAs and their OSCs (namely, NF-OSCs), thanks to their tunable electronic structures and strong optical absorption in the visible and near-infrared bands compared to fullerene acceptors.^{14,15} Accordingly, champion NF-OSCs have now achieved power conversion efficiencies (PCEs) exceeding 18%.^{16,17} Among those high-performing NFAs, one finds IT-4F and related structures; however, the critical issues of relatively large voltage loss and inferior electron transportation to that of holes in paired polymeric donors (*i.e.*, PM6, PTB7-Th, *etc.*) notably stand out, for which n-doping appears a facile solution. Recently, the groups of Anthopoulos and Bao reported the n-doping in NF-OSCs using respective dopants of benzyl viologen (BV) and (12*a*,18*a*)-5,6,12,12*a*,13,18,18*a*,19-octahydro-5,6-dimethyl-13,18[1',2']benzenobisbenzimidazo [1,2*b*:2',1'*d*]benzo [*i*][2.5]benzodiazocine potassium triflate adduct (DMBI-BDZC), which significantly improved molecular packing, balanced charge transport, facilitated exciton dissociation and reduced nongeminate (bimolecular) recombination.^{4,8} While these studies afford a vital guidance for n-doping in NF-OSCs, it would be particularly desirable to obtain more mechanistic understanding.¹³ In the first instance, the light absorption enhancement of the doped active layer is generally described to be a major key to the photocurrent increase, yet the correlation between n-doping and optical absorbance awaits to be clarified.^{4,8} For another, since it is difficult to control the dopant distribution in the layers prepared by directly introducing dopants into the blend solution,^{18,19} the doping effects on exciton generation and diffusion within donor/acceptor (D/A) domains are also noteworthy but far from understood. Such information, however, is indispensable for a deep comprehension of the photo-charge generation process.^{6,7} Not to mention that the gain in higher photocurrent is often at the expense of photovoltage loss in OSCs due to the large energy offset at D/A interface,^{20,21} for which the simultaneously increasing short-circuit current density (J_{SC}) and open-circuit voltage (V_{OC}) found in the above-mentioned n-doped devices has yet to be rationalized.^{4,8}

This contribution is therefore motivated by our interest in gaining further insights into the photovoltaic process in n-doped BHJ layers and the ensuing performance of NF-OSCs. A prototypical n-type dopant (4-(1,3-dimethyl-2,3-dihydro-1*H*-benzimidazol-2-yl)phenyl) dimethylamine (namely, *N*-DMBI) is adopted to dope the benchmark PM6:Y6 blend based NF-OSCs.¹⁶ Given the peculiar doping mechanism *via* hydrogen removal and hydride transfer, *N*-DMBI is featured to dope those hosts without sufficient energy offset by yielding an intermediate radical with an elevated energy level of singly-occupied molecular orbitals (SOMO).²²⁻²⁴ Herein we propose that an optimum *N*-DMBI content can trigger the heterogeneous nucleation of PM6 and/or Y6, functioning as the seeding sites with high surface tension to reduce the thermodynamic barrier for nucleation, and the elongated crystal coherence length

(CCL) is correlated strongly with the enhancement of optical absorbance. By probing charge generation process in both neat and blend films, n-doping is unraveled to retard monomolecular germinate recombination (GR) both at D/A interfaces and within the constituent domains by dilating D/A interspace and reducing structural-defect-mediated recombination, respectively. Remarkably, n-doping in neat Y6 film allows for increased spatial separation of the coulombically bound electron-hole pairs, thereby prolonging exciton lifetime and further suppressing GR. Moreover, the enlarged D/A interspace brought by dopant intercalation decelerates interfacial electron/hole transfer yet the exciton dissociation remains to function effectively at a discreet spatial distance as long as the GR is significantly impeded, which well-interprets the concurrent increase of J_{SC} and V_{OC} in device. Of particular finding is a lower doping concentration results in negligible modulation of the BHJ electronic structures while an excessive doping is destructive to molecular packing, charge transport and exciton splitting, yielding an optimal *N*-DMBI dopant level of 0.005 wt% in this study. As a result, the PCE of the champion *N*-DMBI-doped device is increased from 14.15% to 15.34%, with a significant rise of J_{SC} from 23.83 to 26.41 mA cm⁻² and a moderate improvement of V_{OC} from 0.84 to 0.86 V, as compared to those of the undoped control device. The enhancement is primarily attributed to n-doping induced optical enhancement, more efficient exciton dissociation and less recombination loss.

Results and discussion

In order to incorporate a trace amount of *N*-DMBI, certain volumes of dilute *N*-DMBI chloroform solution at 0.1 mg mL⁻¹ were dripped into the as-prepared solutions of PM6 and Y6. Note the weight percentage of *N*-DMBI in PM6:Y6 was calculated as a fraction of the total blend mass. In such a way it was converted with regards to the neat masses of donor and acceptor for PM6/Y6 solutions in order to make comparable measurement (see details in the Experimental section in the ESI).[†] The chemical structures and energy diagrams of PM6 donor, Y6 acceptor and n-type dopant *N*-DMBI are provided in Fig. 1a, and the optical absorption spectra of both neat and blends in solution and thin film are shown in Fig. 1b. In blend films, the optimized PM6:Y6 weight ratio of 1 : 1.2 is directly drawn from literature, while the *N*-DMBI content is varied from 0, 0.002, 0.005, 0.008, 0.015 to 0.020 wt%.¹⁶ The thicknesses of neat and blend thin films w/o *N*-DMBI are almost identical to each other, as determined by step profilometer measurements (Fig. S1, ESI[†]), which rule out the thickness effect on light absorbance. It can be seen that the absorption profiles of neat PM6:Y6 blend film without *N*-DMBI is nearly a superposition of individual PM6 and Y6 spectra with the main peaks located at 625 and 829 nm, respectively.^{25,26} For all the blend thin films w/o *N*-DMBI, there is no new absorption band or peak shift observed in the spectra, implying the absence of significant chemical reactions between them, which is also supported by the nearly unchanged Fourier-transform infrared (FT-IR) spectra as shown in Fig. S2a, ESI[†]

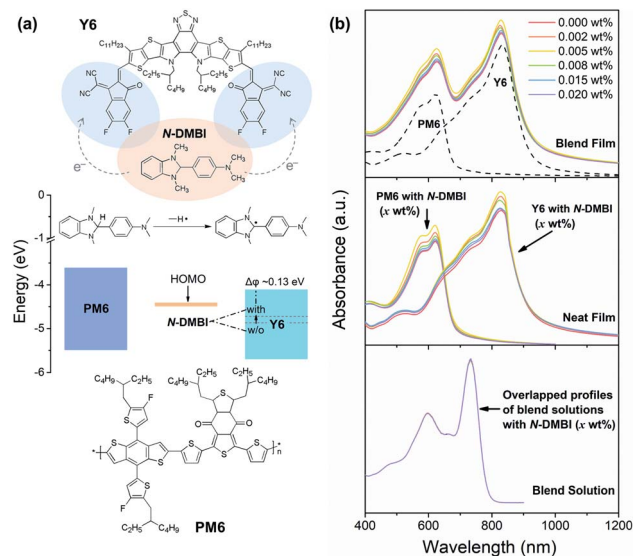


Fig. 1 Materials and optical absorption. (a) Energy level diagram, molecular structures of Y6 acceptor and *N*-DMBI dopant. (b) Light absorption spectra of the PM6:Y6 blend, neat PM6 and Y6 in both thin films and solution with *x* wt% *N*-DMBI content.

Firstly, by adding 0.002 and 0.005 wt% *N*-DMBI into the PM6:Y6 blend, the overall light absorbance is increased gradually, which is pronounced for the shoulder peaks at 570 and 730 nm, indicative of enhanced intermolecular packing. Further increased *N*-DMBI inclusion from 0.008 to 0.02 wt%, in contrast, leads to a steady attenuation of absorbance, presumably suggestive of weakened molecular packing. On the other hand, for neat PM6 and Y6 thin films by adding the same content range of *N*-DMBI, similar absorbance changes are observed. To confirm the aforementioned impact on film structures, the same absorbance in blend solution was measured. From solid to solution, a perceptible bathochromic shift of the spectra indicates strong intermolecular interactions in solid state, and the nearly overlapped spectral profiles implicate the great likelihood of structural modification by *N*-DMBI on thin films. Now the question remains as to how *N*-DMBI molecules modulate thin film structure. In addition, as a typical n-type dopant, the strong electronic interaction between *N*-DMBI and Y6 could also induce local microstructure change in such a way that is differentiated from what might occur in PM6. Therefore, we next attempted to determine whether n-type doping would occur. From Kelvin probe force microscopy (KPFM) measurement, the work function/Fermi level of Y6:*N*-DMBI (0.009 wt%) is up-shifted by 0.13 eV towards the conduction band, giving a direct evidence of effective electron transfer. Moreover, the intensified electronic paramagnetic resonance (EPR) of Y6 doped with 0.005 wt% *N*-DMBI (Fig. S2b, ESI†), and the absent imidazole core hydrogen of *N*-DMBI in the ¹H-NMR spectra (Fig. S2c, ESI†) suggests the formation of *N*-DMBI^{•-} radicals after thermal treatment, which is a signature of such hydride-transfer doping process.^{22–24}

Grazing-incidence wide-angle X-ray scattering (GIWAXS) was employed to gain insight into the molecular packing motifs in

the solution-casted PM6:Y6 blend and PM6/Y6 neat films as a function of *N*-DMBI content. We firstly compare the results with those reported in literature to ensure measurement reliability. As shown in 2D diffractograms (Fig. 2a), the neat PM6 film adopts a preferential face-on orientation to the substrate as evidenced by the stronger diffraction in the out-of-plane (OOP) (101) direction than that in the in-plane (IP) (100) direction. In contrast, the ring-shape pattern of neat Y6 film indicates a more isotropic film structure. In the blend film of PM6 and Y6, the diffraction pattern seems to be mediated by these two constituents, displaying both strong diffraction in OOP and Debye-Scherrer rings. Accordingly, in the linecuts displayed in Fig. 2b, the characteristic peaks were denoted as P_i^{host} for the brevity. Owing to linear π -conjugated backbone and bulky side chains, PM6 possesses a conventional alkyl-to-alkyl diffraction profile, wherein the lamellar stacking of side chains (P_1^{PM6}) is predominant over the π - π stacking (P_2^{PM6}) of backbones.²⁷ For pristine Y6, the characteristic peaks are well-matched with the packing motifs reported in literature,^{28–30} suggesting a mesh-like aromatic structure. The lamellar (P_1^{Y6} and P_2^{Y6}) and π - π stacking peaks (P_3^{Y6} and P_5^{Y6}) here are assigned to the distance of the altered neighboring end-groups and the vertically aligned molecules, respectively.²⁹ Another peak of P_4^{Y6} (0.66 \AA^{-1}) arises from the horizontal backbone-stacking.²⁹ With regards to the pristine blend film, it resembles a mixture of the diffraction pattern of PM6 and Y6, which is characterized by the lamellar and π - π stacking peaks of P_1^{BHJ} and P_5^{BHJ} , respectively. At the same time, the end-group and backbone packing features of Y6— P_2^{BHJ} , P_3^{BHJ} and P_4^{BHJ} —are also preserved in virtue of the mesh structure compactness.

After acquiring results consistent with the literature, we turned our attention to the impact of *N*-DMBI dopant and the correlation with the optical absorbance changes. To quantitatively analyze the dopant position and the domain size, the interplanar distance (namely, *d*-spacing) and coherence length (*i.e.*, L_c) of lamellar and π - π stackings were derived from the position (*q*) and breadth (Δq) of the fitted linecut peaks, according to the relations of $d = 2\pi/q$ and $L_c = 0.89 \times 2\pi/\Delta q$.²⁴ The details of the fitted peaks and the calculated results are shown in Fig. S3–S5 (ESI), Tables S1–S3 (ESI)† and Fig. 3a, respectively. As Fig. 3a shows, the lamellar *d*-spacing of PM6 in OOP direction progressively increases from 19.82 to 20.47 Å with *N*-DMBI content varied from 0 to 11 wt%, while the *d*-space change of lamellar stacking in IP direction and the π - π stacking in either direction are both negligible. Since the edge-on oriented lamellar stacking are minority for PM6, it is plausible to observe less distance change in IP direction. *N*-DMBI dopants are presumed to enter the lamellar interspace because of the spaces provided by the large and flexible alkyl side chains, and thus dilating the interplanar distance. Similarly, the lack of edge-on oriented crystallites and the intrinsically large lamellar *d*-spacing could also explain why L_c changes in IP direction and for lamellar stacking are less distinguishable. In this regard, the biggest increase of L_c from 51.49 to 84.22 Å is observed for the π - π stacking in OOP direction by incorporating 0.011 wt% *N*-DMBI dopant. We think that *N*-DMBI inclusion could give extra steric hindrance to prevent the entanglement of long alkyl side

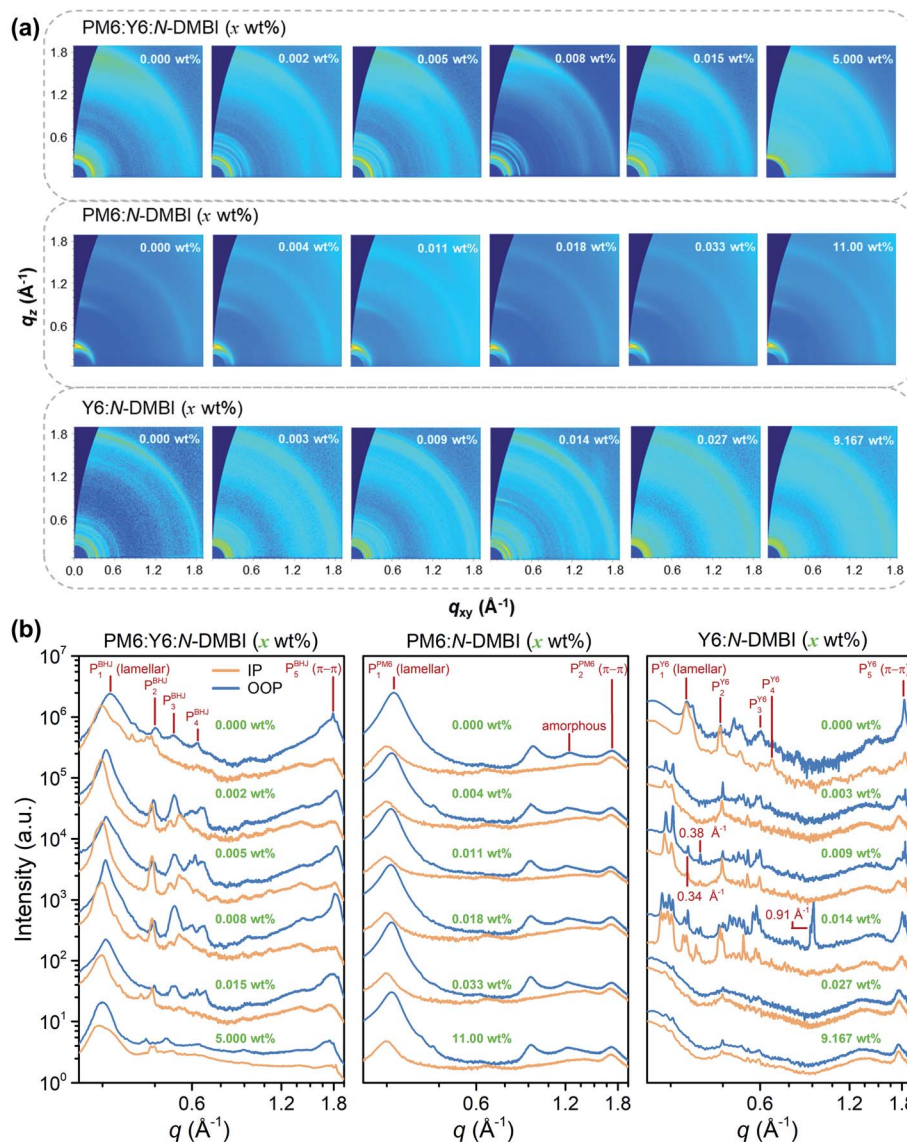


Fig. 2 Microstructure packing motifs. (a) 2D GIWAXS patterns of PM6:Y6, PM6 and Y6 thin films with x wt% N -DMBI. (b) Corresponding 1D linecuts in OOP and IP directions.

chains and hence the reduced lateral bulkiness allow backbones to stack in a longer range.^{31,32} Once adding N -DMBI from 0.018 to 11 wt%, the OOP π - π stacking coherence drops from 75.09 to 58.63 \AA . Since there is no significant change in π - π stacking distance, shortened coherence is attributed to the over-accumulation of N -DMBI within side chains. From the contact angle measurement, the poor miscibility between PM6/Y6 and N -DMBI is evaluated by the high interfacial tension of about 31.19 mN m^{-1} (Fig. S6, Tables S4 and S5 in ESI),[†] indicating the low accessibility of π - π interspace for the insertion of N -DMBI dopant.^{33,34}

Owing to the large interplanar distance and the highly electrophilic end-groups, N -DMBI dopants are also supposed to enter the lamellar interspace of Y6, which is in-between the adjacent end-groups of unpaired molecules. As shown in Fig. 2b and 3a, this is supported by a substantial increase of the OOP

lamellar d -spacing from 18.43 to 21.70, 21.75 and 22.34 \AA by adding 0.003, 0.009 and 0.014 wt% N -DMBI, respectively. High immiscibility between Y6 and N -DMBI is also evidenced by the large interfacial tension of about 25.73 mN m^{-1} from the contact angle measurement. Therefore, the structural ordering could be disrupted and result in the vanishment of lamellar stacking diffractions by introducing more N -DMBI dopant at 0.027 and 9.167 wt%. By tracing back to the linecuts in Fig. 2b, it is found that the lamellar stacking peak (P_1^{Y6}) splits into two sharp peaks for the films doped by 0.003 and 0.009 wt% N -DMBI, and there are even more splits at a higher dopant content of 0.014 wt%. In the case of N -DMBI intercalation as n-type dopant, the refractive index of Y6 film could be spatially varied as a consequence of the local lattice distortion and the electron density redistribution, giving rise to the multiple scattering of diffraction beam and finally leading to the peak

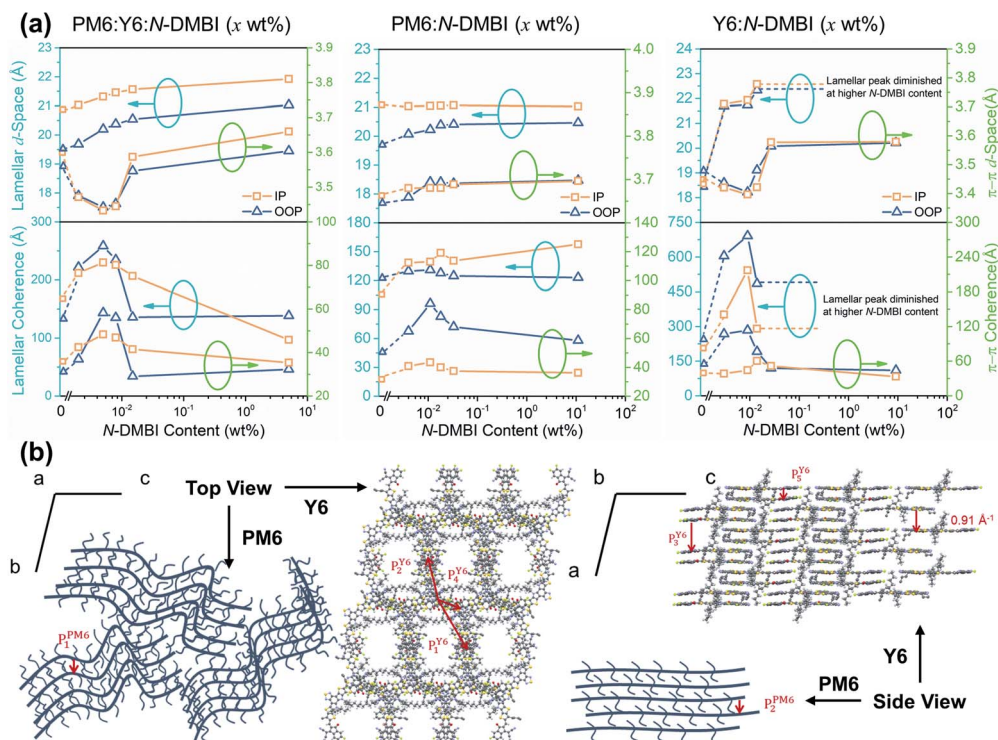


Fig. 3 Quantification of molecular stacking behaviors. (a) Interplanar distance and coherence PM6:Y6, PM6 and Y6 thin films with x wt% N -DMBI derived from the GIWAXS linecuts. (b) Schematic molecular packings of PM6 and Y6, wherein the extended-crystal structures of Y6 are referred to Zhang *et al.*'s work.²⁹

splitting.^{35,36} Notably, for doped films containing 0.009 and 0.014 wt% N -DMBI, the weak peaks at 0.34 and 0.38 \AA^{-1} are assigned to the interaction of ($h00$) planes, and the sharp peak at 0.91 \AA^{-1} may originate from the vacancies created by N -DMBI intercalations, as shown in Fig. 3b.^{29,37} Returning to discuss interplanar distance as shown in Fig. 3a, it is intriguing to note a slight decrease of ~ 0.1 \AA prior to the increase of OOP π - π stacking distance for Y6 with the turning point at 0.009 wt%. By considering the effect of n-type doping, the end-groups of Y6 could be less electropositive after pulling electrons from N -DMB. As a result, the repulsion between the vertically stacked end-groups becomes relieved, thus reducing the π - π stacking distance. Given the less oriented structure, a similar trend of lamellar and π - π stacking d -spacing in IP direction is found for the condensed Y6: N -DMBI (x wt%) films. We recall that the high interfacial energy is also beneficial to the heterogeneous nucleation by reducing the energy barrier for phase transformation. Therefore, the boost of crystallization gives rise to an increasing coherence. As for the PM6:Y6 blend films, on the other side, the lamellar and π - π stacking distance vary with introducing various amounts of N -DMBI by following the same trend as that of neat PM6 and Y6 films, respectively, but the observed values are slightly higher due to the weakened intermolecular interactions by the phase inter-mixing. As the N -DMBI contents are quite low and most of them are supposed to intercalate into the lamellar interspace of PM6 and Y6, the packing behavior of N -DMBI molecules is therefore neglected. We further measured the root-mean-square roughness (RMS) of

the pristine, lightly-doped (0.005 wt%) and heavily-doped (5 wt%) PM6:Y6: N -DMBI films *via* tapping-mode atomic force microscope (TP-AFM) as shown in Fig. S7 (ESI),[†] and the corresponding RMS changes from 0.843 to 1.016 and 0.976 nm, which may arise from the initially enlarged crystal size and the ultimately disordered packing along with the increasing dopant contents. Moreover, the line plots of both lamellar and π - π stacking coherence for blends seem quite similar to that of Y6, but the values are almost halved as the bulk mixing inhibits the domains from growing in the long-range order.

Remarkably, the coherence maxima shown in Fig. 3a are exactly the same point where the films of PM6, Y6 and PM6:Y6 exhibit the highest optical absorbance, and the L_C shows a similar correlation to the optical absorbance with the content of N -DMBI. Based on these results, we believe that the increasing coherence length, or domain size in other words, can effectively reduce the scattering-induced light loss and thus enhancing the overall optical absorbance.

To elucidate the photophysical impact of N -DMBI inclusions on the excited state evolutions in pure domains and at D/A interfaces, transient absorption spectroscopy (TAS) was employed to characterize the exciton recombination behaviors in neat PM6:Y6: N -DMBI and blended PM6:Y6: N -DMBI films. PM6: N -DMBI (x wt%) and Y6: N -DMBI (x wt%) samples were photoexcited by 400 and 800 nm wavelengths with the photon energy slightly above their optical bandgaps respectively, while both wavelengths were used with PM6:Y6: N -DMBI (x wt%) samples to differentiate the dynamic pathways by selectively

exciting individual components. For intuitive comparisons, charge transfer dynamics of each sample were derived from the singular-value-decomposition (SVD) fittings of the measured TAS (Fig. S8, ESI†) as shown in Fig. 4. For the undoped neat PM6/Y6 films, signals of ground-state bleaching (GSB) and excited-state absorption (ESA) appear at 639/887 and 961/971 nm, respectively (Fig. S8a–f, ESI†). For PM6:Y6 blend, 800 nm wavelength can only excite Y6 and produce GSB at 867 nm and ESA at 960 nm (Fig. S8g–i, ESI†), while 400 nm wavelength can excite both PM6 and Y6 and produce signals coinciding to their spectral features (Fig. S8j–l, ESI†).

From the SVD fittings, the PM6:*N*-DMBI (*x* wt%) samples encompass two lifetime components as shown in Fig. 4a–c: GR of the photogenerated excitons (4–27 ns) and non-geminate recombination (NGR) stemming from exciton/polaron annihilation (~30 ps).^{38,39} For Y6:*N*-DMBI (*x* wt%) samples shown in Fig. 4e–g, another component of 1–2 ps besides GR (15–40 ps) and NGR (3–7 ns) is ascribed to the hot carrier cooling and/or the polaron formation in molecules.³⁸ For blend films getting excited by an 800 nm pump shown in Fig. 4i–k, a component of 7–25 ps refers to the hole transfer from Y6 to PM6, wherein the GSB from 650 to 900 nm and positive signal above 600 nm imply the concurrent charge carrier depopulation from Y6 and population at PM6. Another component is featured by the GSB of both PM6 (550–700 nm) and Y6 (650–900 nm), indicating the geminate recombination of the transferred holes in PM6 with the residual electrons in Y6 as shown in Fig. 4l. Similarly, when both Y6 and PM6 are excited by a 400 nm pump (Fig. 4m–o),

another component of 0.2–2 ps is resolved for the process of electron transfer from PM6 to Y6. Pathways of the above excited state evolution and charge transfer are schematically illustrated in Fig. 4d, h, l, p.

Charge generation dynamics of PM6 and Y6 domains within BHJ blends can be similar to what occurs in the corresponding neat films. The fitting results in Fig. 4a–c and e–g suggest a retarded GR in both PM6 and Y6 neat films by incorporating *N*-DMBI dopants, which should be due to the reduction of rapid trap-mediated recombination in the case of better molecular packing.⁴⁰ Of special note is the longest GR of 7.38 ns in heavily-doped Y6 film containing 9.167 wt% *N*-DMBI (Fig. 4g), while the neat PM6 film acquires that of 27.21 ns by incorporating 0.011 wt% *N*-DMBI (Fig. 4c).

Given the peculiar doping effect between Y6 and *N*-DMBI, strong interactions between their frontier orbitals might repel the paired electron and hole in photogenerated excitons, thereby prolonging exciton lifetime with more *N*-DMBI dopant. Moreover, NGR is retarded from 14.87 to 42.64 ns with increasing *N*-DMBI content from 0 to 9.167 wt% in Y6 films (Fig. 4e–g), but it is almost unchanged for the samples of PM6:*N*-DMBI (*x* wt%). From GIWAXS results, *N*-DMBI inclusions exert little impact on the π - π stacking of PM6 but could distort the packing of Y6 due to the interactive end groups for doping. In this case, exciton diffusion is considered to be limited by the lattice distortion in the doped Y6 films, and NGR is therefore retarded as long as excitons cannot encounter with each other and get annihilated.^{41,42} For blend films, GR is

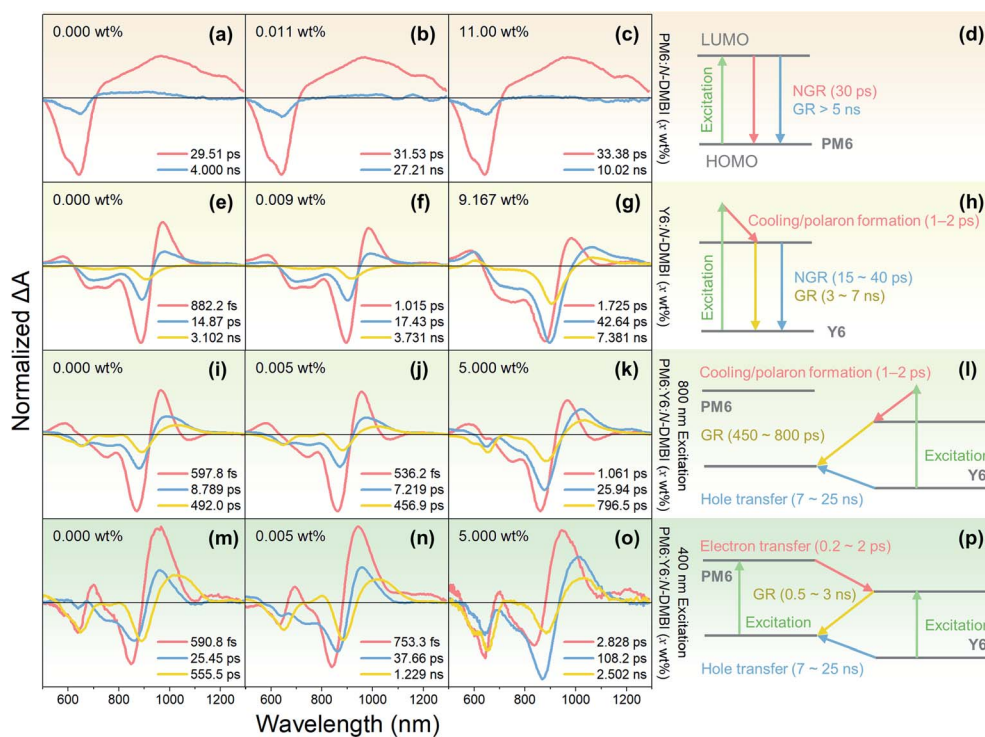


Fig. 4 Thin-film photophysics. SVD fittings of the measured TAS of undoped/doped neat/blend thin films. (a–c) PM6:*N*-DMBI (*x* wt%) excited at 400 nm, (e–g) Y6:*N*-DMBI (*x* wt%) excited at 800 nm, (i–k) PM6:Y6:*N*-DMBI (*x* wt%) excited at 800 nm, and (m–o) PM6:Y6:*N*-DMBI (*x* wt%) excited at 400 nm. (d, h, l, p) Identified schematic pathways of excited-state depopulation for the corresponding neat and blend films.

generally slowed down compared to that in the neat films, implying the efficient exciton dissociation at D/A interfaces. Meanwhile, GR and electron/hole transfer at D/A interface are simultaneously decelerated with the increasing *N*-DMBI content, which could be ascribed to the enlarged D/A interspace by the intercalation of *N*-DMBI dopant.

Finally, we fabricated inverted photovoltaic cells with an ITO/ZnO/PM6:Y6:*N*-DMBI/MoO₃/Ag architecture and correlated the device performance with the impact of *N*-DMBI inclusions in aspects of n-type doping and structural modification. Firstly, the cell performance was optimized by varying the *N*-DMBI

content from 0.002 to 0.005, 0.008, 0.015 and 0.02 wt%. Fig. 5a shows the best-performing *J*-*V* curves for each *N*-DMBI ratios above, and the corresponding photovoltaic parameters are summarized in Table 1. Note that 20 devices were fabricated for each *N*-DMBI concentration to confirm data reproducibility, and their *J*-*V* curves are given in Fig. S9 (ESI).[†] Similar to the optical absorbance and coherence length, the PCE values follow a rise-fall trend with the increasing *N*-DMBI content, in which a vertex of 15.34% is attained at an optimal 0.005 wt% *N*-DMBI, which is ~10% higher than that of undoped device. The remarkable PCE of the champion device benefit primarily from

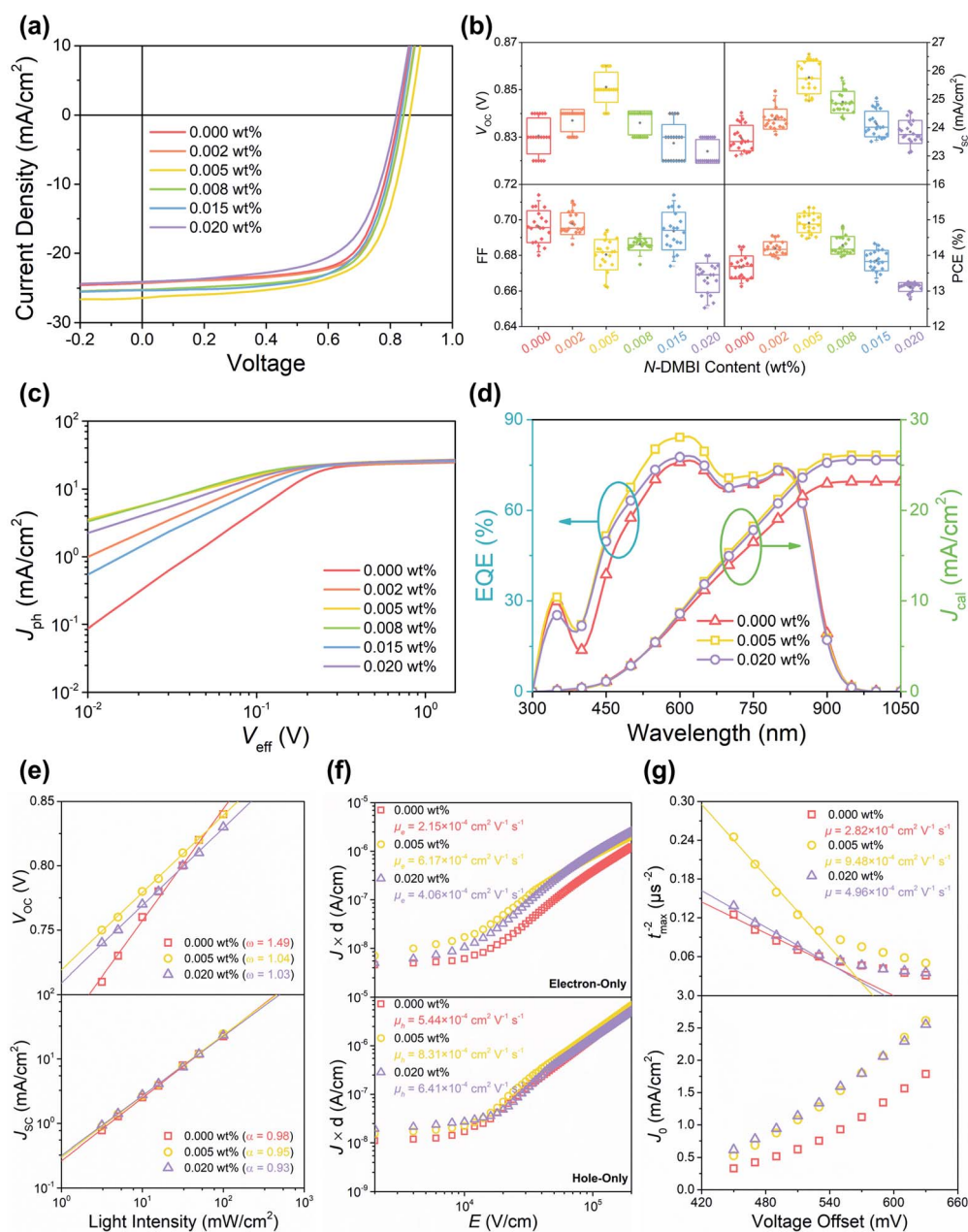


Fig. 5 Photovoltaic device characterization. (a) *J*-*V* curves for PM6:Y6 based OSCs with *x* wt% *N*-DMBI, corresponding (b) statistical distribution of device parameters, (c) *J*_{ph} - *V*_{eff}, (d) EQE profiles, (e) light-intensity dependences of *J*_{sc} and *V*_{oc}, (f) SCLC measurement for electron-only and hole-only devices, and (g) MIM-CELLIV transient *t*_{max} and *j*₀ at varied voltage offsets (see the details in Experimental section in ESI).[†]

Table 1 Summary of the photovoltaic parameters of PM6:Y6 based inverted OSCs with various ratios of *N*-DMBI incorporated

<i>N</i> -DMBI (wt%)	V_{OC} (Avg. \pm Std.) (V)	J_{SC} (Avg. \pm Std.) (mA cm^{-2})	FF (Avg. \pm Std.) (%)	PCE (Avg. \pm Std.) (%)	P_{diss} (%)
0.000	0.84 (0.83 \pm 0.008)	23.83 (23.63 \pm 0.453)	71 (70 \pm 0.9)	14.15 (13.83 \pm 0.319)	96.05
0.002	0.84 (0.84 \pm 0.005)	24.72 (24.30 \pm 0.353)	70 (70 \pm 0.6)	14.51 (14.32 \pm 0.191)	98.39
0.005	0.86 (0.85 \pm 0.006)	26.41 (25.76 \pm 0.579)	68 (68 \pm 0.9)	15.34 (15.07 \pm 0.273)	98.65
0.008	0.84 (0.84 \pm 0.005)	25.75 (24.90 \pm 0.370)	69 (69 \pm 0.3)	14.82 (14.57 \pm 0.252)	97.98
0.015	0.83 (0.83 \pm 0.007)	24.53 (24.13 \pm 0.453)	70 (69 \pm 1.1)	14.25 (13.96 \pm 0.287)	94.06
0.020	0.82 (0.82 \pm 0.005)	24.33 (23.85 \pm 0.410)	66 (67 \pm 1.0)	13.16 (13.04 \pm 0.120)	90.47

the high J_{SC} and V_{OC} of 26.41 mA cm^{-2} and 0.86 V, while the FF of 0.68 is relatively low. The universality of these findings is also supported by the statistical distribution of photovoltaic parameters as shown in Fig. 5b, from which the same rise-fall trend with a common turning point at 0.005 wt% *N*-DMBI is also found for both J_{SC} and V_{OC} . We also fabricated other three NF-OSCs to demonstrate the versatility of *N*-DMBI doping, which were composed of PTB7-Th:ITIC, PTB7-Th:IT-4F and PTB7-Th:IEICO-4F as the photo-active layers in devices. Similar photovoltaic improvement can be observed, and the results are shown in Fig. S10 and Table S6 (ESI).[†] To gain better insights into the evolution of photovoltaic performance, the J_{SC} and V_{OC} will be discussed individually for the three selected devices that are undoped, doped with the optimal and excessive content in the following context.

In terms of J_{SC} , we first estimated the photogenerated current (J_{ph}) from the current density differences under illumination and dark conditions as shown in Fig. 5c and S11 (ESI).[†] From the plot, the exciton dissociation probability (P_{diss}) could be assessed by the ratio of the J_{ph} and saturated current (J_{sat}) at zero applied bias, and the results are listed in Table 1 (see the details in Experimental section). It can be seen that the optimal device with 0.005 wt% *N*-DMBI affords the highest P_{diss} of 98.65%, which subsequently drops to 90.47% by adding 0.02 wt% *N*-DMBI, and this could be rationalized by GIWAXS and TAS results. With increasing *N*-DMBI content, the increasing D/A interspace could effectively retard interfacial GR and the probability of exciton dissociation is therefore raised by the prolonged exciton lifetime. On the other hand, the large interspace caused by excessive dopants could hinder charge transfer at D/A interfaces, which is undesirable to exciton splitting. Moreover, the J_{ph} of the optimized device first arrive at a saturation, which also proves the more efficient charge transport and collection with less electric field dependence.⁴³ In addition to exciton dissociation, the optical absorbance is also intimately related to J_{SC} . To compare the EQE spectra in Fig. 5d, the optimized device with 0.005 wt% *N*-DMBI exhibits the highest photo-response over the full range from 300 to 1050 nm, which is consistent with the optical absorbance in Fig. 1b. From the EQE spectra, the current densities (J_{cal}) of the devices containing 0, 0.005 and 0.02 wt% *N*-DMBI dopant are integrated to be 23.15, 26.05 and 25.55 mA cm^{-2} , respectively, which has a deviation of $\pm 5\%$ relative to the J_{SC} values obtained from J - V measurement. From this point of view, the intensified EQE

photoresponse could be originated from the enhancement of optical absorbance, which also contributes to the rise of J_{SC} .

Since V_{OC} is solely determined by the voltage loss associated with radiative and non-radiative recombination, the light-intensity dependent measurement was performed to investigate the role of *N*-DMBI dopant.⁴⁴ According to the power law, $J_{SC} \propto (P_{in})^\alpha$ and $V_{OC} \propto \omega k_B T / q \ln(P_{in})$, where P_{in} refers to various illumination intensities, k_B is Boltzmann constant, T is absolute temperature, and q is elementary charge. In these two relations, the constants of α and ω describe the short-circuit bimolecular recombination and the open-circuit trap-assisted recombination, respectively.⁴⁵ As shown in Fig. 5e, the optimized device with 0.005 wt% *N*-DMBI dopant possesses both moderate α (0.95) and ω (1.04) values, while the undoped and highly doped devices obtain the α (0.98) and ω (1.03) that are closest to unity, respectively. These results imply that *N*-DMBI dopants could suppress trap-assisted recombination but meanwhile result in more bimolecular recombination. It is commonly regarded that the second-order bimolecular recombination is accomplished by the diffusion of opposite charge carriers toward each other under the coulombic field, while the first-order trap-assisted recombination is much faster since one of the charges is immobilized within the traps. Therefore, the reduced trap-assisted recombination with increasing *N*-DMBI content could be ascribed to the trap filling effect, while the competitive bimolecular recombination is increased concurrently as a result of higher probability of charge carrier annihilation.^{5,11,38,46} Taken together, we find an effective compensation to the α deviation from 0.98 to 0.95 by a remarkable drop of ω from 1.49 to 1.04 when incorporating 0.005 wt% *N*-DMBI dopant. As a result, the total recombination loss is appreciated to be reduced, giving rise to higher V_{OC} . In contrast, the α value is varied constantly to 0.93 at 0.02 wt% *N*-DMBI content yet a decrease of ω is only about 0.01 likely due to the aforementioned poor doping efficiency and less ordered film structure. Therefore, the low V_{OC} is obtained for those devices containing excessive *N*-DMBI dopants.

With regards to FF, the change seems to be irregular for the slightly-doped cells with 0.002, 0.005, 0.008 and 0.015 wt% *N*-DMBI, but a more distinguishable drop of about 0.3 is observed for the device with 0.02 wt% *N*-DMBI as shown in Fig. 5b. To investigate the origin of such variation, we derived the cell series resistance (R_S) and shunt resistance (R_{SH}) from the slopes of the dark J - V curves as shown in Fig. S11 (ESI).[†] First, the R_S are calculated to be 6.45 ± 0.31 , 5.58 ± 0.34 , 4.76 ± 0.40 , $5.71 \pm$

0.42, 6.13 ± 0.32 and $6.45 \pm 0.31 \Omega \text{ cm}^2$, while the R_{SH} are 1.61 ± 0.08 , 2.70 ± 0.12 , 5.26 ± 0.09 , 4.35 ± 0.03 , 3.13 ± 0.12 , and $0.99 \pm 0.04 \text{ K}\Omega \text{ cm}^2$ for the devices contain 0, 0.002, 0.005, 0.008, 0.015 and 0.02 wt% *N*-DMBI, respectively. In terms of R_{S} , it is found to decrease with increasing dopant concentration from 0 to 0.002 and 0.005 wt%, which could be attributed to the general doping effect of increasing charge carrier density. Then, R_{S} gets recovered for the higher *N*-DMBI content, which is ascribed to the more disordered molecular packing. As for the change of R_{SH} , a similar trend was observed due to the variations in leak current. In the case of low doping concentration, the increase in domain (crystal) size could also increase the surface roughness yet lead to poor interfacial contact and high leak current, which are consistent with the TP-AFM results as shown in Fig. S7 (ESI).[†] To combine the effects of both R_{S} and R_{SH} , the FF declines due to the lower R_{SH} for the slightly-doped devices, which might be compensated by the effect of the R_{S} reduction. However, R_{S} cannot keep dropping while R_{SH} could turn to decrease when there are excessive dopants to impair the orderliness of molecular packing. That probably explains why the change in FF seems to be more random in the slightly-doped devices yet more severe in the heavily-doped device.

Stability is always concerned for the n-type doping due to its reactive nature, and hence we performed the stability test for the non-encapsulated devices in N_2 -filled glovebox. As shown in Fig. S12 (ESI),[†] the stability of the doped cells is comparable to that of the pristine cell, and all of them can retain more than 85% efficiency after 288 h storage, even for the device that contain high dopant content of 0.02 wt%. These results indicate that the inclusion of small amount of *N*-DMBI has negligible effects on device stability.

In parallel, a series of electrical measurements were conducted to complement the above photoelectrical characterization. Space-charge-limited current (SCLC) measurements were performed to determine charge carrier mobility, which also reflects the bimolecular recombination of charge carriers in dark condition. For the electron-only and hole-only devices containing 0, 0.005 and 0.02 wt% *N*-DMBI, the J - V curves and corresponding mobilities are shown in Fig. 5f (see the details in Experimental section in ESI).[†] In accordance with the longest OOP π - π stacking coherence revealed by the previous GIWAXS measurement, the well-developed charge transport pathways afford the highest electron mobility (μ_{e}) of $6.17 \times 10^{-4} \text{ cm}^2 \text{ V}^{-1} \text{ s}^{-1}$ and hole mobility (μ_{h}) of $8.31 \times 10^{-4} \text{ cm}^2 \text{ V}^{-1} \text{ s}^{-1}$ for the champion device with 0.005 wt% *N*-DMBI dopant (see the details in Experimental section in ESI).[†] According to Langevin theory, bimolecular recombination constant (k_{L}) can be described by an equation of $k_{\text{L}} = q (\varepsilon_0 \varepsilon_{\text{r}})^{-1} (\mu_{\text{e}} + \mu_{\text{h}})$, where q is elementary charge, ε_0 and ε_{r} are the vacuum and relative dielectric constants, respectively. Compared with the light intensity-dependent results, it appears to be contradictory for the optimized device to obtain a moderate α yet the highest mobilities. For one thing, the charge transportation is the most balanced with $\mu_{\text{e}}/\mu_{\text{h}}$ of 0.74 in the optimized device, suggesting the less space-charge accumulation for the undesired bimolecular recombination.⁸ For another, given the reduced π - π stacking distance as shown in Fig. 3a, the molecular

polarizability is supposed to rise, thus giving higher ε_{r} .⁴⁷ To validate this argument, we further utilized the technique of metal-insulator-metal charge extraction by linearly increasing voltage (MIM-CELIV) to qualitatively assess the dielectric properties of the devices.⁴⁸⁻⁵⁰ The extracted current maximum (t_{max}) and the displacement current plateau (j_0) of each transient current peak are plotted in Fig. 5g as a function of voltage offset, and the specific dark MIM-CELIV transients are shown in Fig. S13 (ESI).[†] The μ_{CELIV} values derived from the slope of t_{max} are on the order of $10^{-4} \text{ cm}^2 \text{ V}^{-1} \text{ s}^{-1}$, among which the optimized cell displays the highest μ_{CELIV} of $9.48 \times 10^{-4} \text{ cm}^2 \text{ V}^{-1} \text{ s}^{-1}$, in good agreement with the above SCLC mobilities. Most of all, the conjecture of increasing ε_{r} is evidenced by the high j_0 of the optimized device according to the relation of $j_0 \propto \varepsilon_{\text{r}}$.⁴⁸ In short, both balanced carrier transportation and higher molecular polarizability could mitigate the bimolecular recombination loss for the best-performing device with 0.005 wt% *N*-DMBI dopant.

Conclusions

In conclusion, we have systematically investigated n-doping of the BHJ active layers in NF-OSCs to reveal the origins of enhanced optical absorbance, prolonged exciton lifetime and simultaneously increasing J_{SC} and V_{OC} . On account of high interfacial energy, a small amount of *N*-DMBI dopant is incorporated to trigger the crystallization of PM6/Y6 films and the enlarged CCL derived from molecular packing motifs, in accordance with the enhancement of optical absorbance. With regard to photophysics, GR in neat PM6/Y6 films is retarded by included *N*-DMBI dopant, which we attribute to the mitigated structural defects, and the possibly less strongly bound excitons, in particular with Y6. For PM6:Y6 blends, a deceleration of both GR and charge transfer at D/A interface is primarily ascribed to the increasing D/A interspace caused by *N*-DMBI intercalation. Meanwhile, an optimum P_{diss} suggests that exciton dissociation is most effective at a discrete D/A distance wherein GR is significantly suppressed, which explains the simultaneous increase of J_{SC} and V_{OC} in device with an optimal *N*-DMBI content, delivering a best efficiency exceeding 15.3%. We believe these findings are critical to comprehend the underlying mechanisms of n-doping in but not limited to PM6:Y6 based NF-OSCs.

Conflicts of interest

There are no conflicts to declare.

Acknowledgements

The work was financially supported by National Natural Science Foundation of China (NSFC) – The Swedish Foundation for International Cooperation in Research and Higher Education (STINT) under grant No. 52011530126, and the Science and Technology Commission of Shanghai Municipality (STCSM) under grants No. 20XD1400500 and 21520710900 (Z. L.). K. Z. acknowledges the support by Danish Council for Independent

Research No. 7026-0037B and Swedish Research Council No. 2017-05337. The authors also thank for the beam time and technical supports provided by BL14B1 GIWAXS and BL01B FT-IR beamlines at Shanghai Synchrotron Radiation facility (SSRF). The authors would like to thank Shiyanjia Lab (<https://www.shiyanjia.com>) for KPFM and EPR measurement.

References

- H. Yan and W. Ma, *Nat. Mater.*, 2019, **18**, 1266–1277.
- I. Salzmänn, G. Heimel, M. Oehzelt, S. Winkler and N. Koch, *Acc. Chem. Res.*, 2016, **49**, 370–378.
- F. Deschler, E. Da Como, T. Limmer, R. Tautz, T. Godde, M. Bayer, E. von Hauff, S. Yilmaz, S. Allard, U. Scherf and J. Feldmann, *Phys. Rev. Lett.*, 2011, **107**, 127402.
- D. Li, F. Geng, T. Hao, Z. Chen, H. Wu, Z. Ma, Q. Xue, L. Lin, R. Huang, S. Leng, B. Hu, X. Liu, J. Wang, H. Zhu, M. Lv, L. Ding, M. Fahlman, Q. Bao and Y. Li, *Nano Energy*, 2022, **96**, 107133.
- G. Zuo, Z. Li, O. Andersson, H. Abdalla, E. Wang and M. Kemerink, *J. Phys. Chem. C*, 2017, **121**, 7767–7775.
- H. Yan, Y. Tang, X. Sui, Y. Liu, B. Gao, X. Liu, S. F. Liu, J. Hou and W. Ma, *ACS Energy Lett.*, 2019, **4**, 1356–1363.
- W. Xue, Y. Tang, X. Zhou, Z. Tang, H. Zhao, T. Li, L. Zhang, S. Liu, C. Zhao, W. Ma and H. Yan, *Adv. Funct. Mater.*, 2021, **31**, 2101892.
- Y. Lin, Y. Firdaus, M. I. Nugraha, F. Liu, S. Karuthedath, A. H. Emwas, W. Zhang, A. Seitkhan, M. Neophytou, H. Faber, E. Yengel, I. McCulloch, L. Tsetseris, F. Laquai and T. D. Anthopoulos, *Adv. Sci.*, 2020, **7**, 1903419.
- F. Pallini, S. Mattiello, M. Cassinelli, P. Rossi, S. Mecca, W. L. Tan, M. Sassi, G. Lanzani, C. R. McNeill, M. Caironi and L. Beverina, *ACS Appl. Energy Mater.*, 2022, **5**, 2421–2429.
- A. F. Paterson, L. Tsetseris, R. Li, A. Basu, H. Faber, A. H. Emwas, J. Panidi, Z. Fei, M. R. Niazi, D. H. Anjum, M. Heeney and T. D. Anthopoulos, *Adv. Mater.*, 2019, **31**, 1900871.
- Z. Shang, T. Heumueller, R. Prasanna, G. F. Burkhard, B. D. Naab, Z. Bao, M. D. McGehee and A. Salleo, *Adv. Energy Mater.*, 2016, **6**, 1601149.
- A. Veysel Tunc, A. De Sio, D. Riedel, F. Deschler, E. Da Como, J. Parisi and E. von Hauff, *Org. Electron.*, 2012, **13**, 290–296.
- H. Yan and W. Ma, *Adv. Funct. Mater.*, 2021, **32**, 2111351.
- Y. Lin, J. Wang, Z. G. Zhang, H. Bai, Y. Li, D. Zhu and X. Zhan, *Adv. Mater.*, 2015, **27**, 1170–1174.
- C. Yan, S. Barlow, Z. Wang, H. Yan, A. K.-Y. Jen, S. R. Marder and X. Zhan, *Nat. Rev. Mater.*, 2018, **3**, 18003.
- J. Yuan, Y. Zhang, L. Zhou, G. Zhang, H.-L. Yip, T.-K. Lau, X. Lu, C. Zhu, H. Peng, P. A. Johnson, M. Leclerc, Y. Cao, J. Ulanski, Y. Li and Y. Zou, *Joule*, 2019, **3**, 1140–1151.
- T. Zhang, C. An, P. Bi, Q. Lv, J. Qin, L. Hong, Y. Cui, S. Zhang and J. Hou, *Adv. Energy Mater.*, 2021, **11**, 2101705.
- Y. Tang, B. Lin, H. Zhao, T. Li, W. Ma and H. Yan, *ACS Appl. Mater. Interfaces*, 2020, **12**, 13021–13028.
- Z. Chen, Y. Tang, B. Lin, H. Zhao, T. Li, T. Min, H. Yan and W. Ma, *ACS Appl. Mater. Interfaces*, 2020, **12**, 25115–25124.
- D. Qian, Z. Zheng, H. Yao, W. Tress, T. R. Hopper, S. Chen, S. Li, J. Liu, S. Chen, J. Zhang, X. K. Liu, B. Gao, L. Ouyang, Y. Jin, G. Pozina, I. A. Buyanova, W. M. Chen, O. Inganas, V. Coropceanu, J. L. Bredas, H. Yan, J. Hou, F. Zhang, A. A. Bakulin and F. Gao, *Nat. Mater.*, 2018, **17**, 703–709.
- J. Yuan, T. Huang, P. Cheng, Y. Zou, H. Zhang, J. L. Yang, S.-Y. Chang, Z. Zhang, W. Huang, R. Wang, D. Meng, F. Gao and Y. Yang, *Nat. Commun.*, 2019, **10**, 570.
- P. Wei, J. H. Oh, G. D. Dong and Z. Bao, *J. Am. Chem. Soc.*, 2010, **132**, 8852–8853.
- Y. Zeng, W. Zheng, Y. Guo, G. Han and Y. Yi, *J. Mater. Chem. A*, 2020, **8**, 8323–8328.
- C. Y. Yang, Y. F. Ding, D. Huang, J. Wang, Z. F. Yao, C. X. Huang, Y. Lu, H. I. Un, F. D. Zhuang, J. H. Dou, C. A. Di, D. Zhu, J. Y. Wang, T. Lei and J. Pei, *Nat. Commun.*, 2020, **11**, 3292.
- W. Liu, Q. Liu, C. Xiang, H. Zhou, L. Jiang and Y. Zou, *Surf. Interface Anal.*, 2021, **26**, 101385.
- G. Wen, R. Hu, X. Su, Z. Chen, C. Zhang, J. Peng, X. Zou, X. He, G. Dong and W. Zhang, *Dyes Pigm.*, 2021, **192**, 109431.
- L. Zhu, M. Zhang, G. Zhou, T. Hao, J. Xu, J. Wang, C. Qiu, N. Prine, J. Ali, W. Feng, X. Gu, Z. Ma, Z. Tang, H. Zhu, L. Ying, Y. Zhang and F. Liu, *Adv. Energy Mater.*, 2020, **10**, 1904234.
- S. Marina, A. D. Scaccabarozzi, E. Gutierrez-Fernandez, E. Solano, A. Khirbat, L. Ciammaruchi, A. Iturraspe, A. Balzer, L. Yu, E. Gabirondo, X. Monnier, H. Sardon, T. D. Anthopoulos, M. Caironi, M. Campoy-Quiles, C. Müller, D. Cangialosi, N. Stingelin and J. Martin, *Adv. Funct. Mater.*, 2021, **31**, 2103784.
- G. Zhang, X. K. Chen, J. Xiao, P. C. Y. Chow, M. Ren, G. Kupgan, X. Jiao, C. C. S. Chan, X. Du, R. Xia, Z. Chen, J. Yuan, Y. Zhang, S. Zhang, Y. Liu, Y. Zou, H. Yan, K. S. Wong, V. Coropceanu, N. Li, C. J. Brabec, J. L. Bredas, H. L. Yip and Y. Cao, *Nat. Commun.*, 2020, **11**, 3943.
- R. Zhou, Z. Jiang, C. Yang, J. Yu, J. Feng, M. A. Adil, D. Deng, W. Zou, J. Zhang, K. Lu, W. Ma, F. Gao and Z. Wei, *Nat. Commun.*, 2019, **10**, 5393.
- Y. Ma, D. Cai, S. Wan, P. Yin, P. Wang, W. Lin and Q. Zheng, *Natl. Sci. Rev.*, 2020, **7**, 1886–1895.
- M. Bajpai, R. Srivastava, R. Dhar and R. S. Tiwari, *Mater. Sci. Eng., B*, 2016, **212**, 62–70.
- P. Bi, S. Zhang, Z. Chen, Y. Xu, Y. Cui, T. Zhang, J. Ren, J. Qin, L. Hong, X. Hao and J. Hou, *Joule*, 2021, **5**, 2408–2419.
- H. Chen, R. Zhang, X. Chen, G. Zeng, L. Kobera, S. Abbrent, B. Zhang, W. Chen, G. Xu, J. Oh, S.-H. Kang, S. Chen, C. Yang, J. Brus, J. Hou, F. Gao, Y. Li and Y. Li, *Nat. Energy*, 2021, **6**, 1045–1053.
- R. Resel, M. Bainschab, A. Pichler, T. Dingemans, C. Simbrunner, J. Stangl and I. Salzmänn, *J. Synchrotron Radiat.*, 2016, **23**, 729–734.
- N. Mrkyvkova, P. Nadazdy, M. Hodas, J. Chai, S. Wang, D. Chi, M. Sojkova, M. Hulman, A. Chumakov, O. V. Kononov, A. Hinderhofer, M. Jergel, E. Majkova, P. Siffalovic and F. Schreiber, *Cryst. Growth Des.*, 2020, **20**, 5269–5276.

- 37 H. W. Cho, N. G. An, S. Y. Park, Y. S. Shin, W. Lee, J. Y. Kim and S. Song, *Adv. Energy Mater.*, 2020, **10**, 1903585.
- 38 B. Wu, X. Wu, C. Guan, K. Fai Tai, E. K. Yeow, H. Jin Fan, N. Mathews and T. C. Sum, *Nat. Commun.*, 2013, **4**, 2004.
- 39 C. M. Proctor, M. Kuik and T.-Q. Nguyen, *Prog. Polym. Sci.*, 2013, **38**, 1941–1960.
- 40 Z. Li, W. Wang, N. C. Greenham and C. R. McNeill, *Phys. Chem. Chem. Phys.*, 2014, **16**, 25684–25693.
- 41 J. Gorenflot, M. C. Heiber, A. Baumann, J. Lorrman, M. Gunz, A. Kampgen, V. Dyakonov and C. Deibel, *J. Appl. Phys.*, 2014, **115**, 144502.
- 42 Q. Zhou, J. Duan, J. Du, Q. Guo, Q. Zhang, X. Yang, Y. Duan and Q. Tang, *Adv. Sci.*, 2021, **8**, 2101418.
- 43 Z. Liu, *Org. Electron.*, 2021, **93**, 106153.
- 44 X. Chen, D. Qian, Y. Wang, T. Kirchartz, W. Tress, H. Yao, J. Yuan, M. Hülsbeck, M. Zhang, Y. Zou, Y. Sun, Y. Li, J. Hou, O. Inganäs, V. Coropceanu, J. L. Bredas and F. Gao, *Nat. Energy*, 2021, **6**, 799–806.
- 45 T. A. Dela Peña, J. I. Khan, N. Chaturvedi, R. Ma, Z. Xing, J. Gorenflot, A. Sharma, F. L. Ng, D. Baran, H. Yan, F. Laquai and K. S. Wong, *ACS Energy Lett.*, 2021, **6**, 3408–3416.
- 46 H. Yan, J. G. Manion, M. Yuan, F. P. Garcia de Arquer, G. R. McKeown, S. Beaupre, M. Leclerc, E. H. Sargent and D. S. Seferos, *Adv. Mater.*, 2016, **28**, 6491–6496.
- 47 X. Zhang, C. Li, J. Xu, R. Wang, J. Song, H. Zhang, Y. Li, Y.-N. Jing, S. Li, G. Wu, J. Zhou, X. Li, Y. Zhang, X. Li, J. Zhang, C. Zhang, H. Zhou, Y. Sun and Y. Zhang, *Joule*, 2022, **6**, 1–14.
- 48 M. Stephen, K. Genevičius, G. Juška, K. Arlauskas and R. C. Hiorns, *Polym. Int.*, 2017, **66**, 13–25.
- 49 S. Züfle, S. Altazin, A. Hofmann, L. Jäger, M. T. Neukom, T. D. Schmidt, W. Brütting and B. Ruhstaller, *J. Appl. Phys.*, 2017, **121**, 175501.
- 50 R. Hanfland, M. A. Fischer, W. Brütting, U. Würfel and R. C. I. MacKenzie, *Appl. Phys. Lett.*, 2013, **103**, 063904.